Supporting Information

Comment on "Bioinspired Reversible Switch between Underwater Superoleophobicity/Superaerophobicity and Oleophilicity/Aerophilicity and Improved Antireflective Property on the Nanosecond Laser-Ablated Superhydrophobic Titanium Surfaces"

Peter Gregorčič

Faculty of Mechanical Engineering, University of Ljubljana, Aškerčeva 6, Ljubljana 1000, Slovenia

Corresponding author:

* E-mail: peter.gregorcic@fs.uni-lj.si (P. Gregorčič)

Table of Contents

S6. ToF-SIMS Analysis

S7. Light Reflection from the Metallic Surface

S8. Light Reflection from the Metallic Surface Covered by a Single Thin-Film Layer

S9. Light Reflection from the Metallic Surface Covered by Double Thin-Film Layer

S10. References

S1   Chemical Composition of the Titanium Sample

The chemical composition of the titanium samples used in the supplementary experiments was assessed using X-ray fluorescence spectrometer (Thermo Scientific Niton XL3t GOLDD+) and is listed in Table S1. The titanium alloy with this chemical composition is classified as Ti-6Al-4V (also known as TC4 or Ti64).

In the paper by Lian et al.,[S1] the authors determined the chemical composition of their sample using energy-dispersive X-ray spectroscopy (EDS) with the following results recorded before laser texturing: 86.7% Ti, 6.5% Al, 3.3% V and 3.5% O. Since the X-ray fluorescence spectrometer used in the experiments supporting this study is not able to detect the O element, the results by Lian et al.[S1] were normalized to Ti, Al, and V elements (excluding the O element) for a more consistent comparison. The normalized results are shown in the last row of Table S1.

Table S1. Chemical composition of the titanium sample (before laser processing) used in this study and in the study by Lian et al.[S1] (in wt. %).

Element	Ti	Al	V	Fe
This study	89.3	6.2	4.3	0.16
Lian et al.,[S1] normalized to Ti, Al, V	89.8	6.7	3.4	/

S2   Low-Temperature Annealing

The titanium-alloy samples labeled S1 and S2 were firstly laser-textured utilizing the parameters listed in the main text. Afterwards, they were low-temperature annealed in the air atmosphere at normal pressure in furnaces, shown in Figure S1.

Figure S1. Photography of **a** Furnace #1, **b** Furnace #2 and **c** Furnace #3.

S3 Measurements of the Total Volatile Organic Compounds (TVOC) Concentration

The concentration of total volatile organic compounds (TVOC) was measured by using PID-AH2 photoionization detector (Alphasense Ltd.) that is able to detect VOC with ionization potential < 10.6 eV. The detector was calibrated by isobutylene and it was placed inside all three furnaces at room temperature as it cannot be used at temperatures above 55 °C. The TVOC concentrations in $\mu g/m^3$ of the isobutylene equivalent as a function of time are shown in Figure S2. The signals are changing by time due to the equalization of the TVOC concetration inside and outside the furnace as well as due to different atmospheric conditions in the laboratory (e.g., opening of the windows and doors etc.). The sharp spikes can be considered as sensor noise. Nevertheless, it is evident that Furnace #1 has the lowest measured TVOC concentration.

The Furnace #1 is located in the basement of the Faculty of Mechanical Engineering, Ljubljana, Slovenia (46°02'49.3"N 14°29'56.1"E), while the Furnaces #2 and #3 are located in the *same* room at the ground floor of the Institute of Metals and Technology, Ljubljana, Slovenia (46°02'43.0"N 14°29'44.0"E), near the workshop which is the most probable reason for the increased VOC contamination.

The TVOC measurements in Furnace #1 were performed from 2:45 p.m., February 11th 2020 to 6:45 a.m., February 12th 2020, local time.

The TVOC measurements in Furnace #2 were performed from 8:15 a.m., February 13th 2020 to 7:45 a.m. February 14th 2020, local time.

The TVOC measurements in Furnace #3 were performed from 3:15 p. m., February 12nd 2020 to 3:15 p.m., February 13th 2020, local time.

For orientation, the regulation in Slovenia suggest that under normal conditions the TVOC concentration in offices should not exceed 600 µg/m^3 emitted from the building material (excluding the human emission or the emission of the human activity that may increase this value).
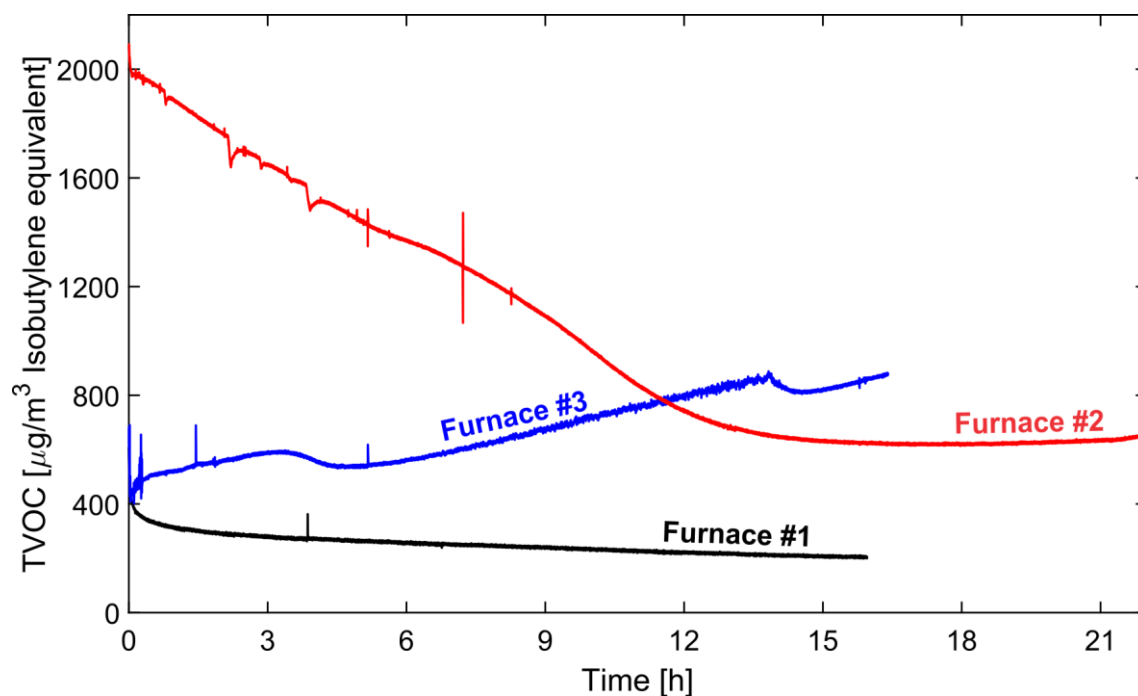
Figure S2. TVOC concentration measurements inside the used furnaces.

S4   Wettability of the Laser-Textured Titanium Alloy

Figure S3 shows the labeling of the samples after each step of the annealing experiments.

The samples were prepared twice:

> ➢ The first set of the samples was prepared within the period of December 18th–20th 2019 (labeled as *Period #1*).
> ➢ The second set of the samples was prepared within the period of February 10th–12th 2020 (labeled as *Period #2*).

The wettability of samples S1 and S2 (from the *Period #1*) immediately after the laser texturing are shown in Figure S4. After several seconds, the whole surface was wet (not shown in the images). The same result was observed on the samples S1 and S2 from the *Period #2*.

The low-temperature annealing of sample S1 in the *contaminated* Furnace #1 for 24 h at 100 °C resulted in a superhydrophobic surface with a contact angle of $161.2° \pm 4.6°$ and roll-off angle of $15.3° \pm 5°$. All the contact angle measurements on the sample S1.1 from *Period #1* are presented in Figure S5, while the raw data is listed in Tables S2 and S3. Similar results were measured on two additional S1.1 samples (A and B), prepared within *Period #2*. Their contact angle measurements are shown in Figure S6. The measurements from the *Period #2* give the contact angle of $156.5° \pm 2°$ and the roll-off angle of $20.4° \pm 3°$. The reason for slightly different wettability as from the *Period #1* might be due to different humidity (during contact angle measurements) or due to slightly different surface contamination.

In the next step, the superhydrophobic surface S1.1 and the fresh, superhydrophilic surface S2 were annealed *together* for 24 h at 100 °C in the *contaminant-free* Furnace #2. After this procedure they are labeled as S1.2 and S2.2.

The surface S2.2 (from *Period #1)* stayed superhydrophilic, as shown in Figure S7. Here, a thin water film spreads over the majority of the surface 2 s after a water droplet is put into contact with the surface, although the whole surface is not wetted at this time. Nevertheless, almost the entire surface is wet after > 2 min (Figure S8). Thus, this surface can still be classified as superhydrophilic and in the saturated Wenzel regime[S2-S4] with a contact angle of zero degrees.

Lower surface wickability (in comparison to the sample S2) most probably arises due to cross-contamination, since the sample S2.2 was annealed together with the contaminated (superhydrophobic) sample S1.2. The same result was also observed on the surface S2.2 from *Period #2*.

However, surface S1.2 (from *Period #1*) stayed hydrophobic with the contact angle of 159.3° ± 2.2° (see Figure S9 and Table S2), but a desorption of the hydrophobic layer must have already started, since the surface became "sticky". Its roll-off angle increased significantly, as revealed by the raw data in Table S3.

The same result is observed for the matching sample prepared and analyzed in *Period #2*. Here, the contact angle of the sample S1.2 equals 152.8° ± 1.9° (Figure S10) and its surface – again – became "sticky" (see Tables S2 and S3). Thus, the wettability of this sample is also consistently lower as that of the sample S1.1, prepared within the same period. Only sample A was analyzed here, since sample B was used for the XPS analysis after the first annealing step in Furnace #1.

Samples S1.2 and S2.2 were simultaneously annealed further for 2 h at 350 °C in Furnace #3 and labeled as S1.3 and S2.3 after the annealing process. Higher temperature successfully modified the contaminated (hydrophobic) surface layer, since both samples *returned* to the initial superhydrophilic state (Figures S11 and S12). Although a water droplet spreads over the enitre surface after several seconds on both samples (not shown in Figures S11 and S12), a difference in wickability of individual surfaces exists. The wickability of the S1.3 (previously significantly contaminated) surface is slightly lower than that of the S2.3 (almost uncontaminated) surface indicating that it is likely that not all the surface hydrophobic contaminants were removed in these 2 h.
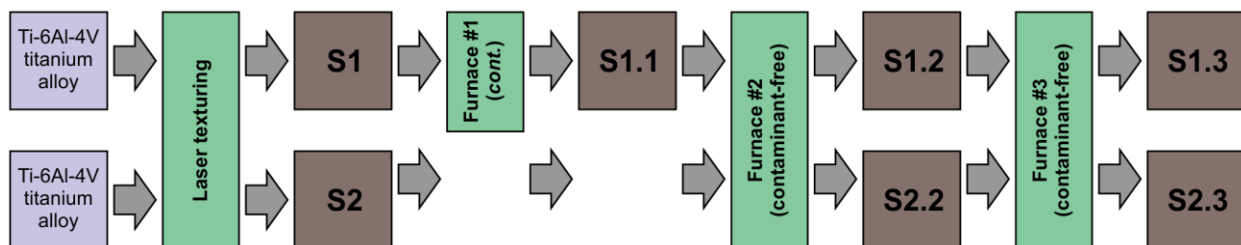
Figure S3. A diagram showing the labeling of the samples (within a single period).
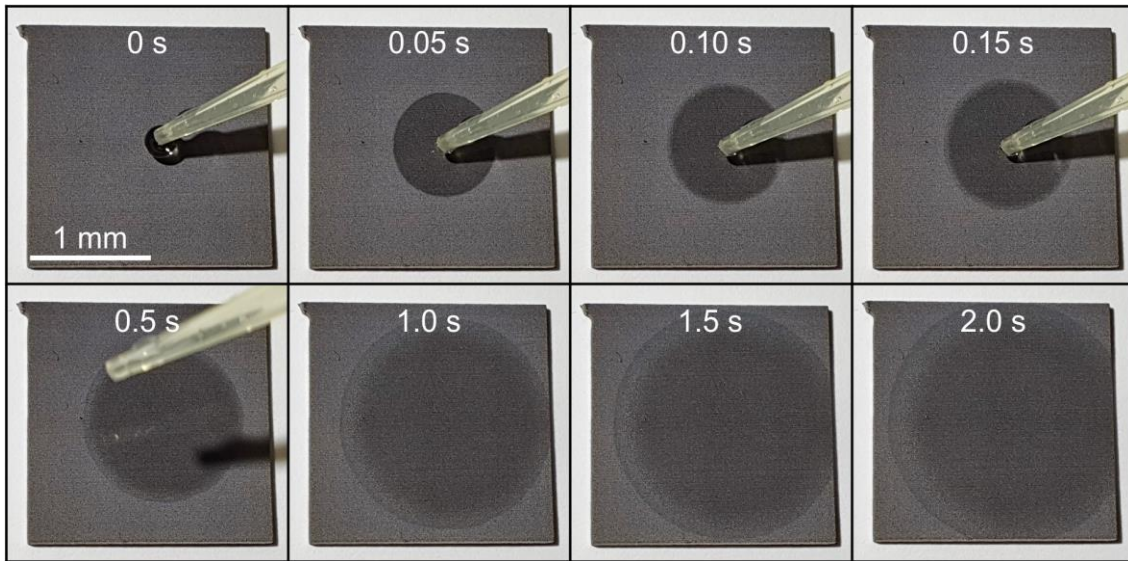
Figure S4. Water spreading immediately after the laser texturing on samples S1 and S2.
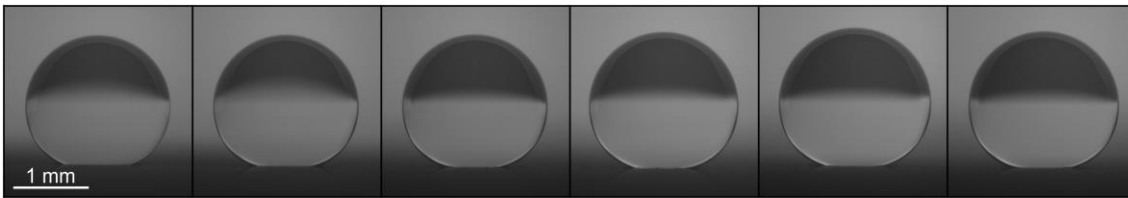
Figure S5. Contact angle measurements on the surface S1.1 (from *Period #1*) after annealing at 100 °C for 24 h in a *contaminated* Furnace #1. Six measurements at different locations on the surface of the *same* sample are shown.
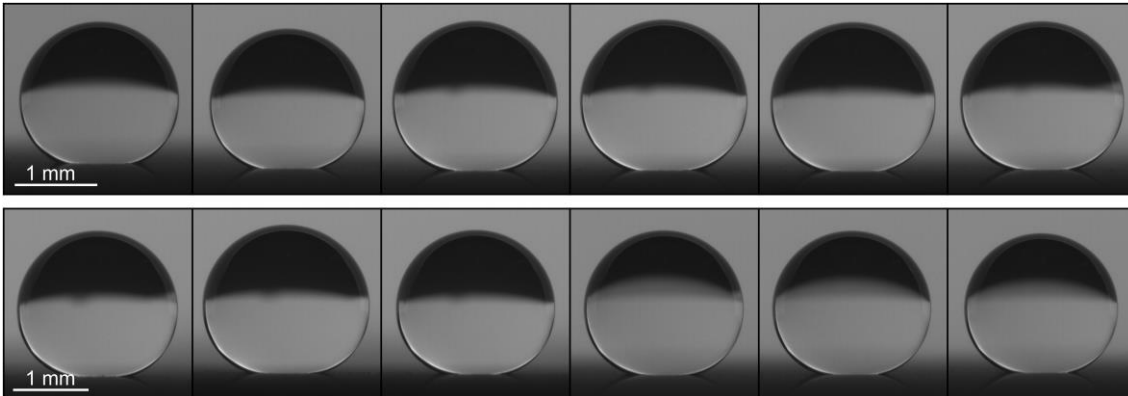
Figure S6. Contact angle measurements on the surface S1.1 (from *Period #2*) after annealing at 100 °C for 24 h in a *contaminated* Furnace #1. Six measurements at different locations on the sample A (top row) and the sample B (bottom row) are shown.
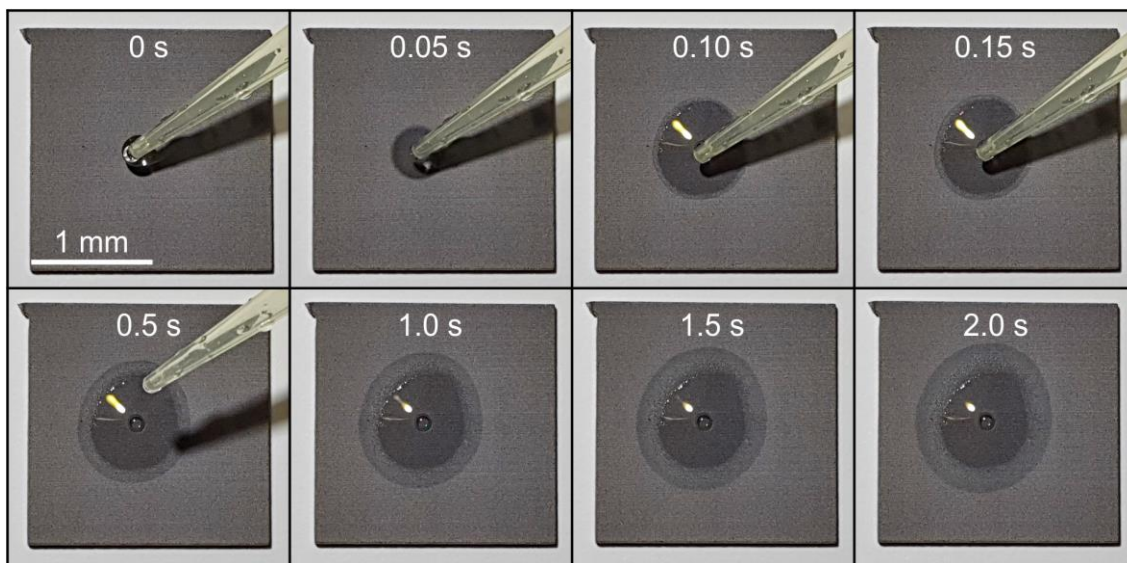
Figure S7. Water spreading on the S2.2 surface after annealing at 100 °C for 24 h (annealed together with the hydrophobic (contaminated) sample S1.2) in Furnace #2. A small water droplet stays in the center of the wet area.

Figure S8. The same sample as in Figure S7 after longer observation times.
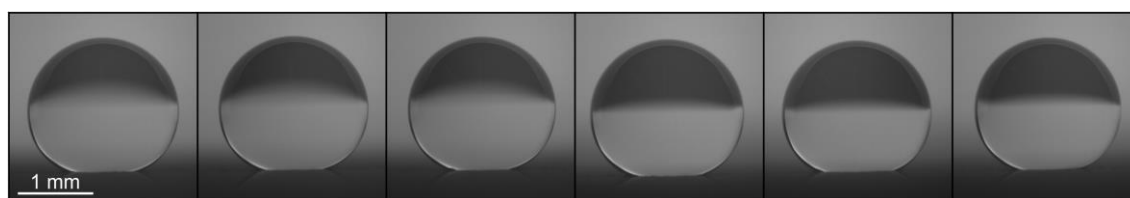
Figure S9. Contact angle measurements on the surface S1.2 (from *Period #1*) after additional 24 h of annealing at 100 °C in a *contaminant-free* Furnace #2. Six measurements at different locations on the surface of the *same* sample are shown.
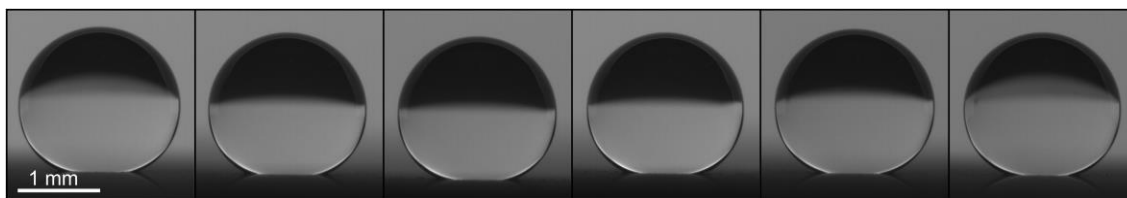
Figure S10. Contact angle measurements on the surface S1.2 (from *Period #2*, sample A) after additional 24 h of annealing at 100 °C in a *contaminant-free* Furnace #2. Six measurements at different locations on the surface of the *same* sample are shown.
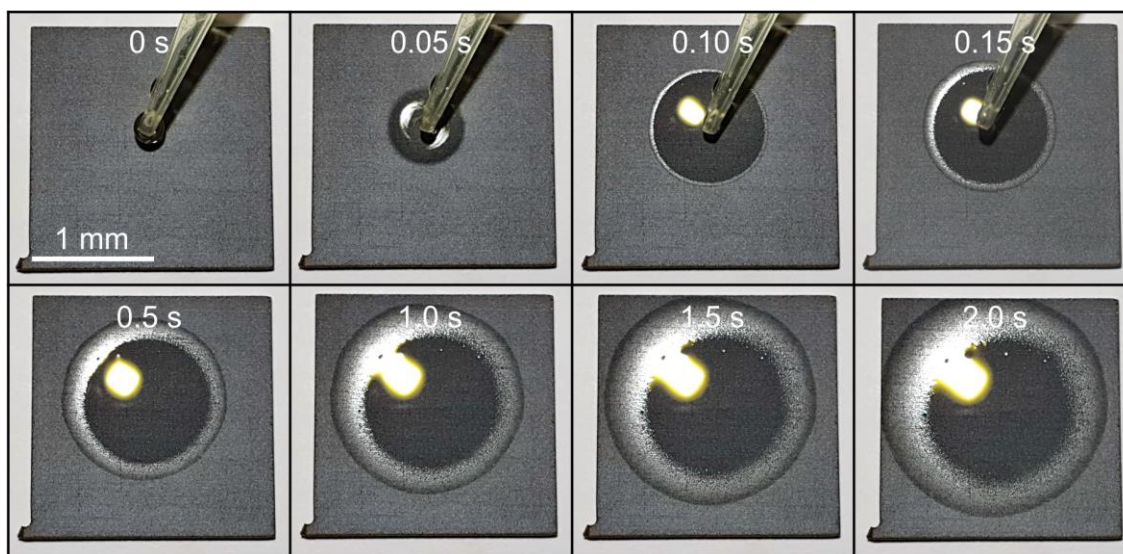
Figure S11. Water spreading on the S1.3 surface after additional 2 h of annealing at 350 °C (in the *contaminant-free* Furnace #3) that turned off the hydrophobicity and returned the sample into the initial superhydrophilic state.
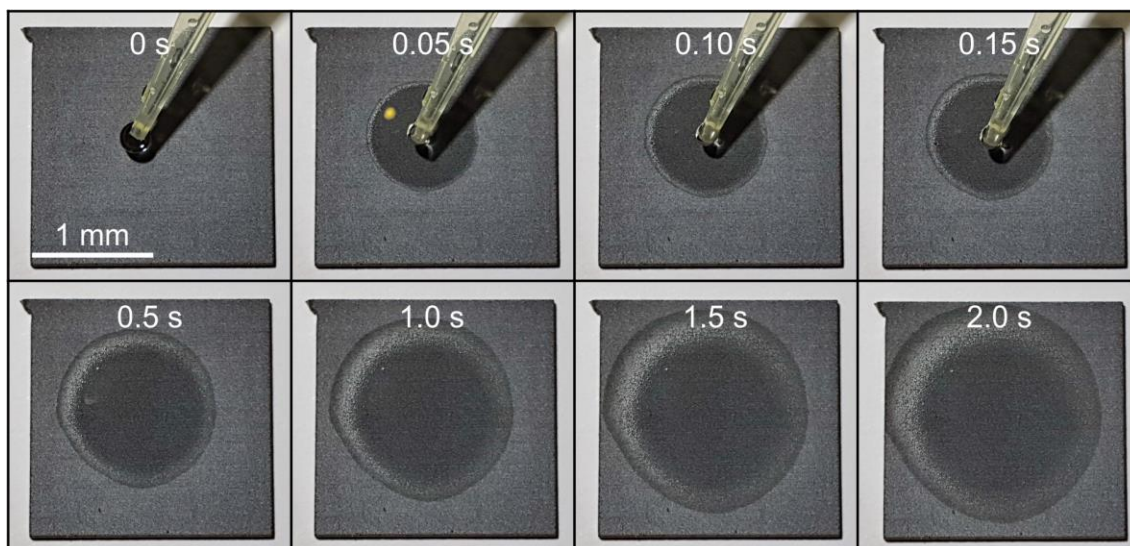
Figure S12. Water spreading on the S2.3 surface after additional 2 h of annealing at 350 °C (in the *contaminant-free* Furnace #3).

Table S2. Contact angles for the hydrophobic samples (all six measurements per sample are shown).

Sample	#1	#2	#3	#4	#5	#6
S1.1 after 24 h @ 100 °C in the *contaminated* Furnace #1, from *Period #1*	152.4°	161.0°	165.9°	162.4°	163.1°	162.7°
S1.1 after 24 h @ 100 °C in the *contaminated* Furnace #1, from *Period #2*, sample A	152.0°	157.7°	160.1°	156.3°	157.5°	155.8°
S1.1 after 24 h @ 100 °C in the *contaminated* Furnace #1, from *Period #2*, sample B	157.1°	155.7°	157.6°	158.3°	154.9°	155.3°
S1.2 after additional 24 h @ 100 °C in the *contaminant-free* Furnace #2, from *Period #1*	159.1°	161.3°	161.4°	156.5°	156.8°	160.6°
S1.2 after additional 24 h @ 100 °C in the *contaminant-free* Furnace #2, from *Period #2*, sample A	153.2°	151.2°	153.3°	150.1°	155.7°	153.6°

Table S3. The roll-off angles for the hydrophobic samples (all eight measurements per sample are shown).

Sample	#1	#2	#3	#4	#5	#6	#7	#8
S1.1 after 24 h @ 100 °C in the *contaminated* Furnace #1, from *Period #1*	15°	14°	22°	11°	15°	9°	24°	12°
S1.1 after 24 h @ 100 °C in the *contaminated* Furnace #1, from *Period #2*, sample A	20°	22°	22°	19°	26°	19°	18°	16°
S1.1 after 24 h @ 100 °C in the *contaminated* Furnace #1, from *Period #2*, sample B	22°	20°	21°	14°	25°	24°	16°	23°
S1.2 after additional 24 h @ 100 °C in the *contaminant-free* Furnace #2, from *Period #1*	NA	NA	NA	32°	78°	NA	29°	NA
S1.2 after additional 24 h @ 100 °C in the *contaminant-free* Furnace #2, from *Period #2,* sample A	NA	58°	NA	NA	60°	NA	NA	NA

S5   XPS Analysis

XPS analysis was performed on samples S1, S1.1, S1.2, S2.2, and S1.3 from *Period #2.* All samples were put into the XPS vacuum chamber within 3 h of fabrication.

The survey spectra were acquired on the as-prepared samples and after a 3 min sputtering by Ar^+ ions, which removed ~ 3 nm of the top surface layer. The survey spectra before the sputtering are shown in Figures S13–S17. The analyzed peaks (O 1s, Ti 2p, N 1s, C 1s, and Si 2p) are labeled.

All the XPS spectra are calibrated using the C 1s peak of 284.6 eV.

The survey spectra were used to determine the concentration of the analyzed elements before and after the Ar^+ sputtering. The results are shown in Table S4 (the contact angle is also added for comparison). Note that the laser-textured surfaces are rough and thus sputtering removes the surface layer more efficiently from the tops than from the valleys of the rough surface.

Figure S18 shows the narrow-scan XPS photopeak for O 1s, measured on the sample S1 (immediately after the laser texturing). The shoulder at the higher binding energies of the O 1s peak can be deconvoluted by a peak at 533.5 eV characteristic for water molecules adsorbed to

TiO$_2$ (the shaded area in Figure S18).[S5-S6] Here, the Shirley-type background was used and the concentration of the H$_2$O was estimated by using an asymmetric curve shape comprised of 60% of Gaussian and 40% of Lorentzian functions, defined as GL(40) in CasaXPS software. As shown in the main text, this shoulder disappears after annealing.

The C 1s peaks were analyzed and deconvoluted. They were fitted using four peaks, corresponding to hydrocarbon chains and the graphitic structure (C-C/C-H, positioned at 284.6 eV), and three functional groups representing the absorption of alcohols/ether group (C-O, ΔBE = +1.5 eV from the main peak), aldehydes/ketones (C=O, ΔBE = +2.7 eV from the main peak) and carboxyl/ester group (O-C=O, ΔBE = +4.3 eV from the main peak).[S7] Again, the Shirley-type background and the GL(40) curve shapes were used for fitting. The XPS spectra are shown in Figures S19–S23, while the concertation of the C-C/C-H compounds in C 1s peak is given in Table S5. The contact angle is added for comparison.

A nitrogen N 1s peak is observed on the laser-textured surfaces before annealing (samples S1 and S2), as shown in Figure S24. This peak is deconvoluted using a linear background and two GL(40) peaks. The first one, centered at 407.3 eV, corresponds to NO$_3$, while the second one, centered at 400.5 eV, is due to the NO species.[S6] The origin of the N 1s peak is most likely the laser-induced plasma during the laser texturing. As shown in the main text, this peak disappears after annealing.

After annealing in Furnace #1, an Si 2p peak appeared on the sample S1.1. The analysis using a linear background and GL(40) peak reveals that it is centered at 101.8 eV (Figure S25). It has been shown[S8-S9] that this peak corresponds to the hydrophobic polymer polydimethylsiloxane (PDMS). The same peak is also observed on the sample S1.2 (Figure S26, centered at 101.9 eV). A significantly lower peak is also detected on the sample S2.2 (Figure S27, centered at 101.7 eV). Here, it most probably appears due to cross contamination, since the contaminated sample S1.1 and the freshly textured sample S2 were annealed together in the *contaminant-free* Furnace #2.

Note that Figures S25-S27 have different binding-energy ranges and, thus, the Si 2p peaks are not visually aligned.

Figure S28 reveals that after annealing at 350 °C in Furnace #3, the Si 2p peak on the sample S1.3 is shifted towards higher binding energies (102.5 eV) indicating the oxidation of PDMS.
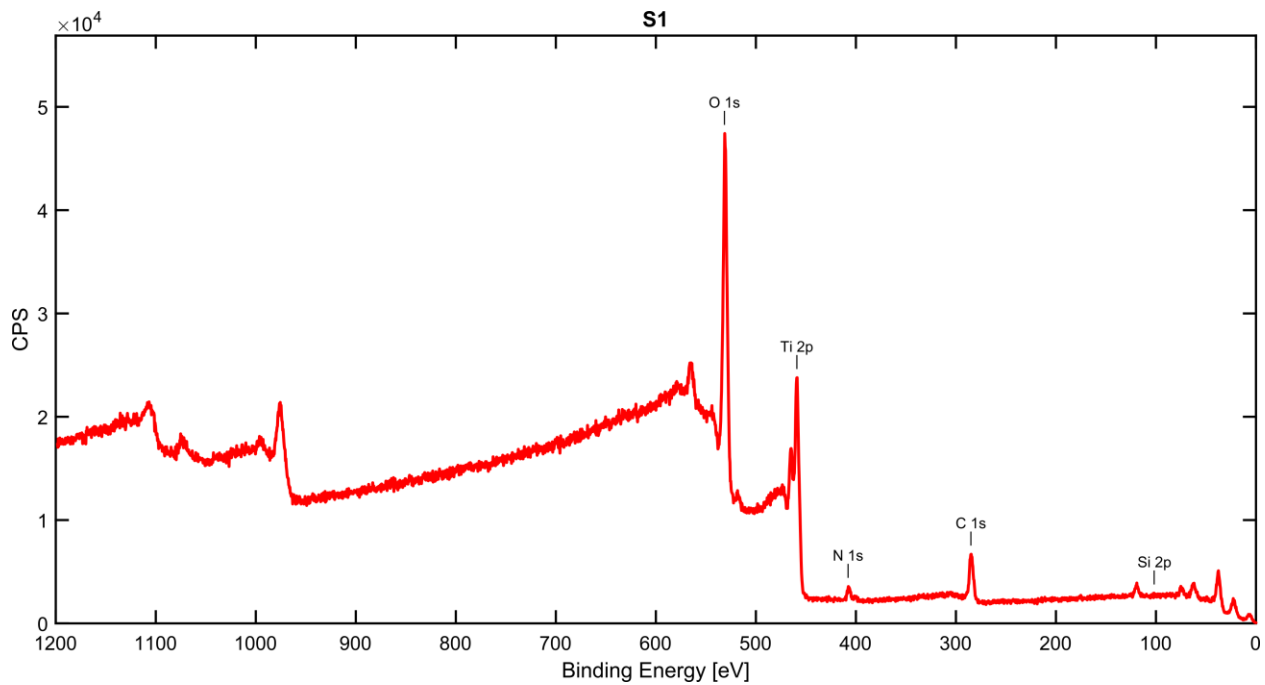
Figure S13. XPS survey spectrum on the sample S1.
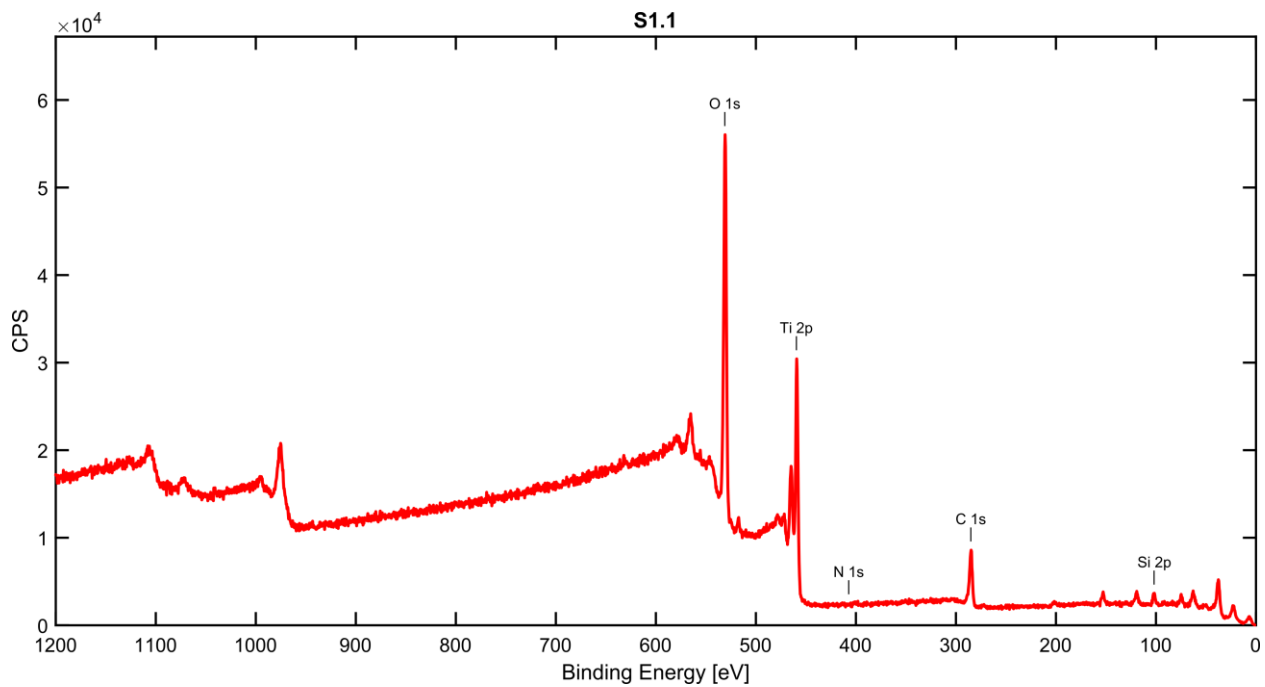
Figure S14. XPS survey spectrum on the sample S1.1.
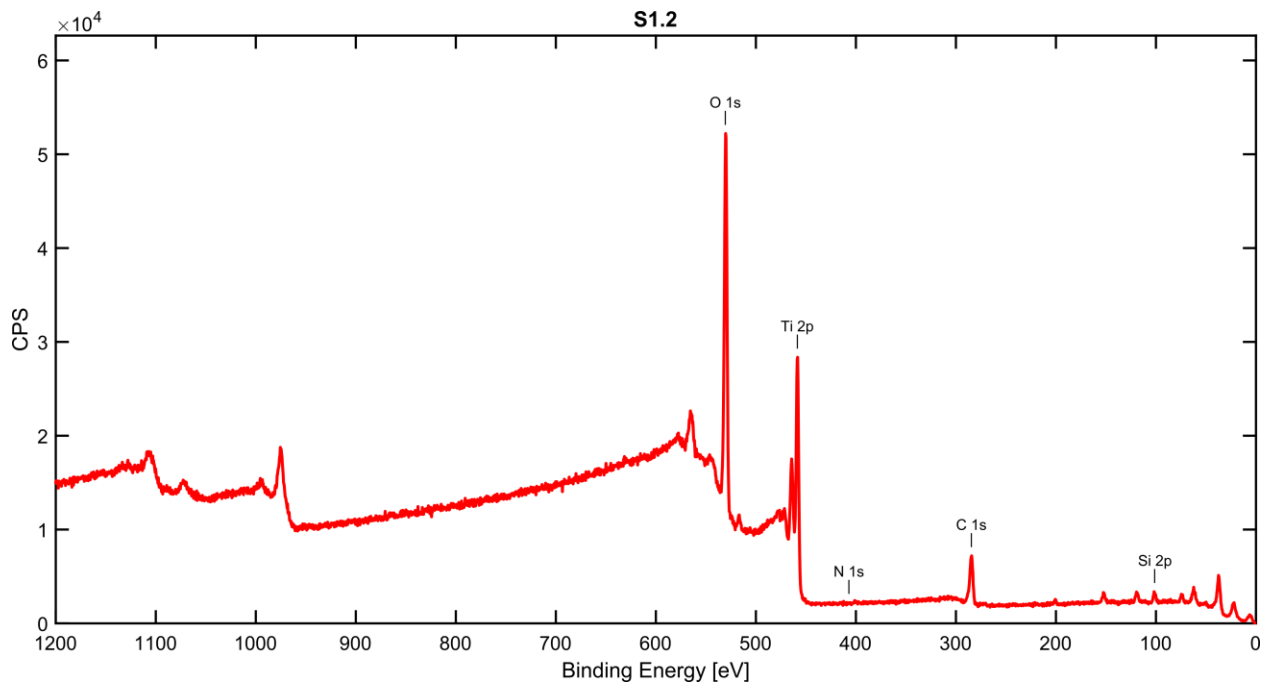
Figure S15. XPS survey spectrum on the sample S1.2.
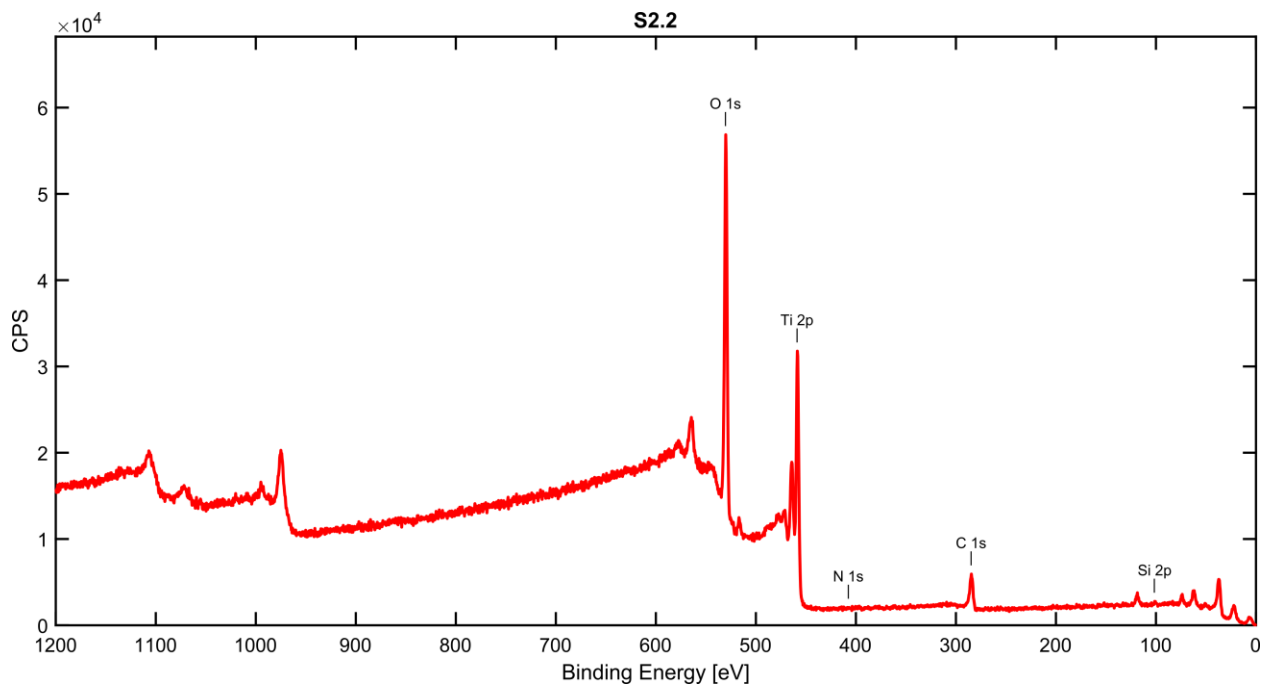
Figure S16. XPS survey spectrum on the sample S2.2.
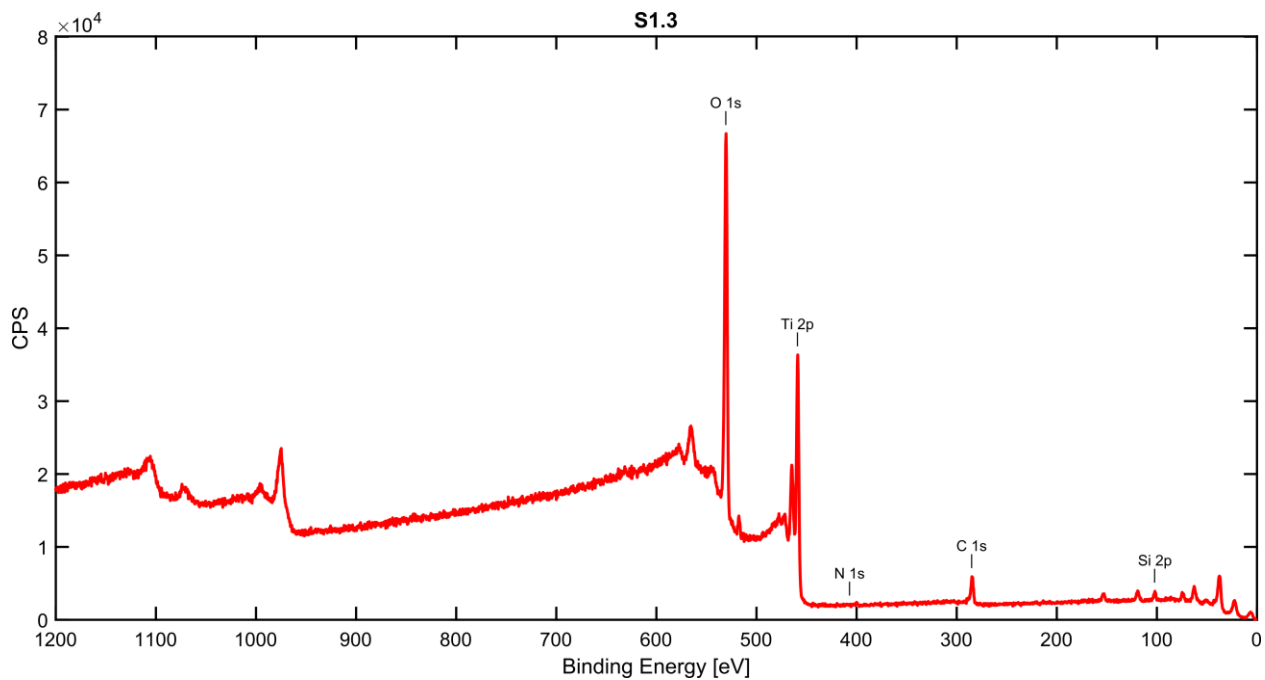
Figure S17. XPS survey spectrum on the sample S1.3.
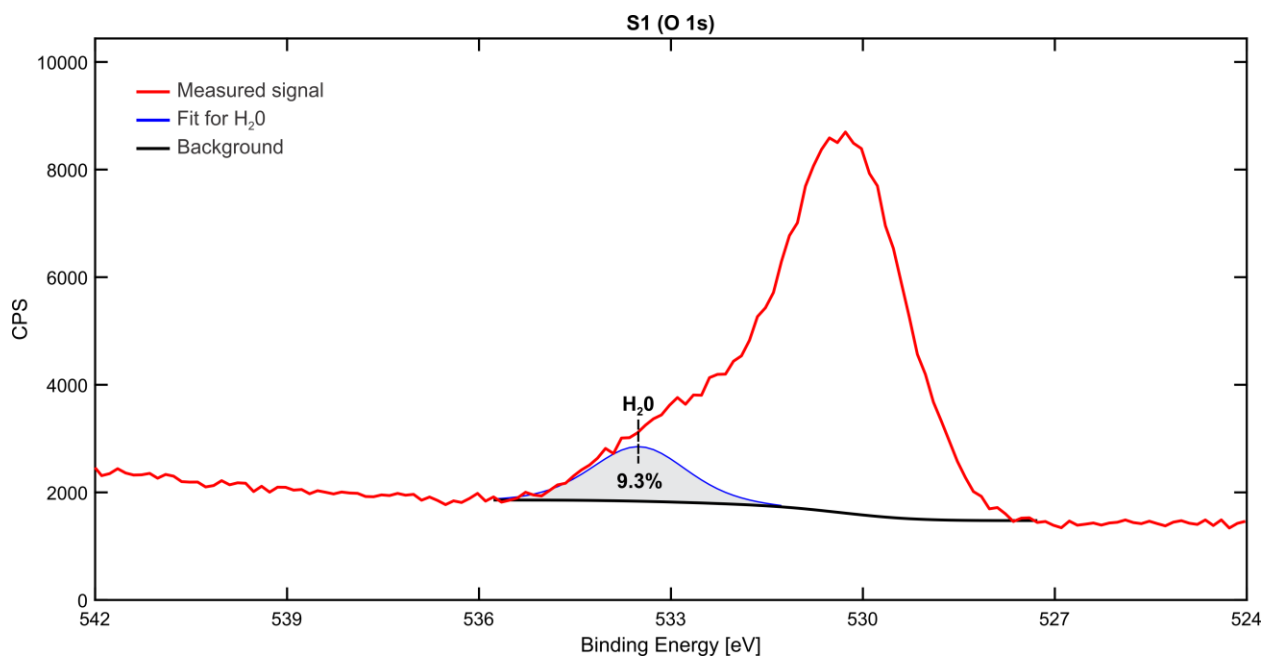
Figure S18. XPS spectrum of the O 1s peak on the sample S1.
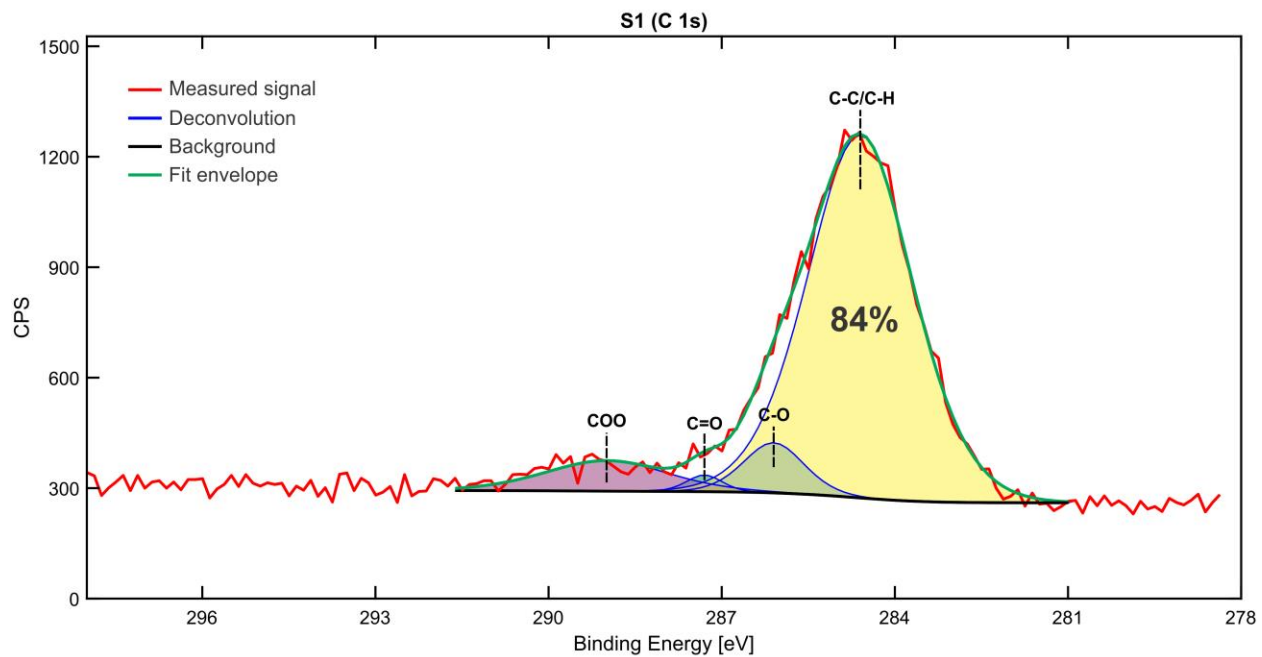
Figure S19. XPS spectrum of the C 1s peak on the sample S1.
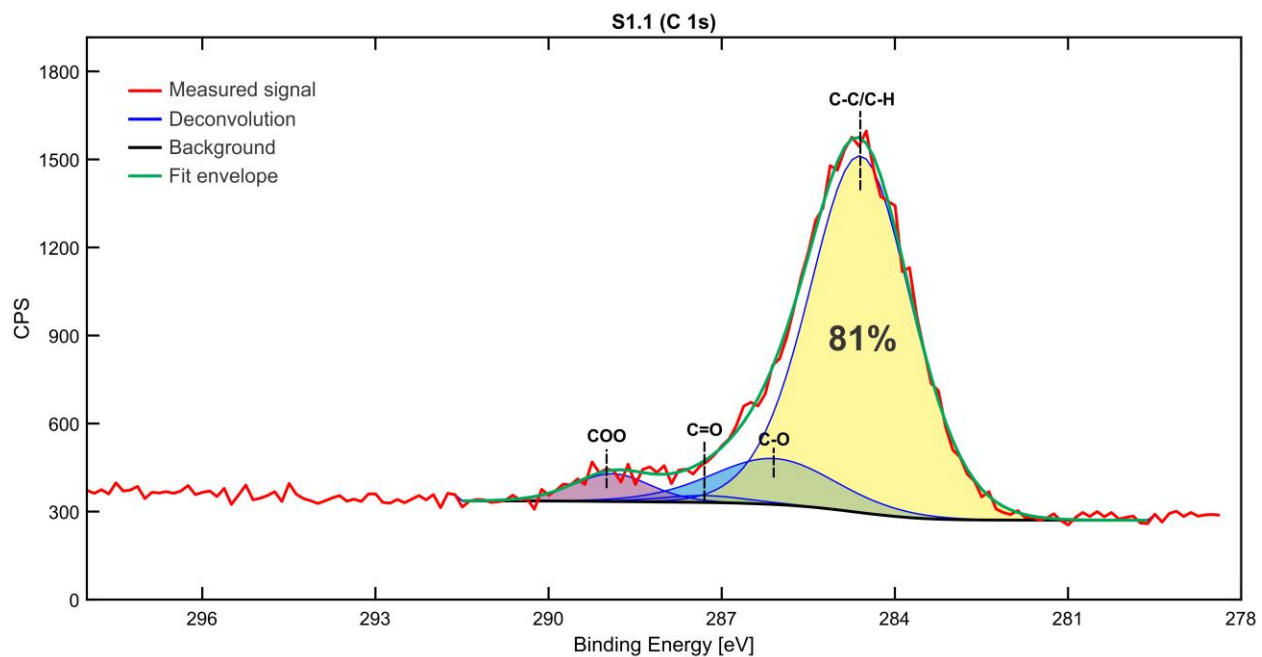
Figure S20. XPS spectrum of the C 1s peak on the sample S1.1.
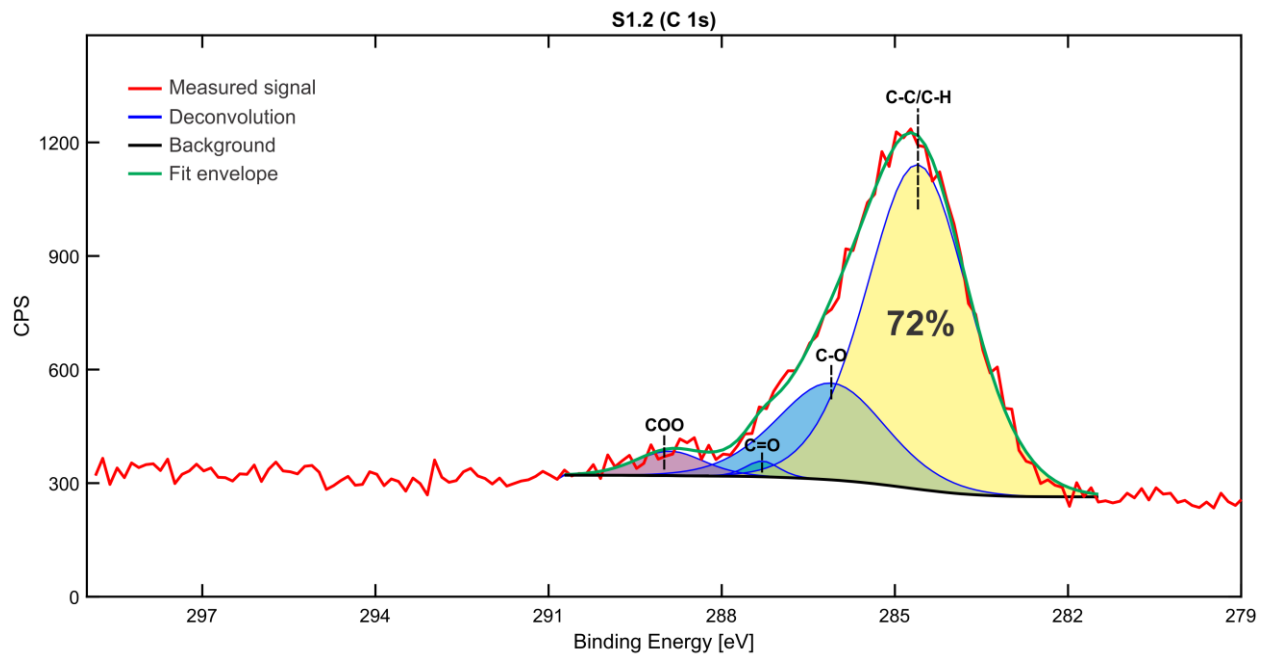
Figure S21. XPS spectrum of the C 1s peak on the sample S1.2.
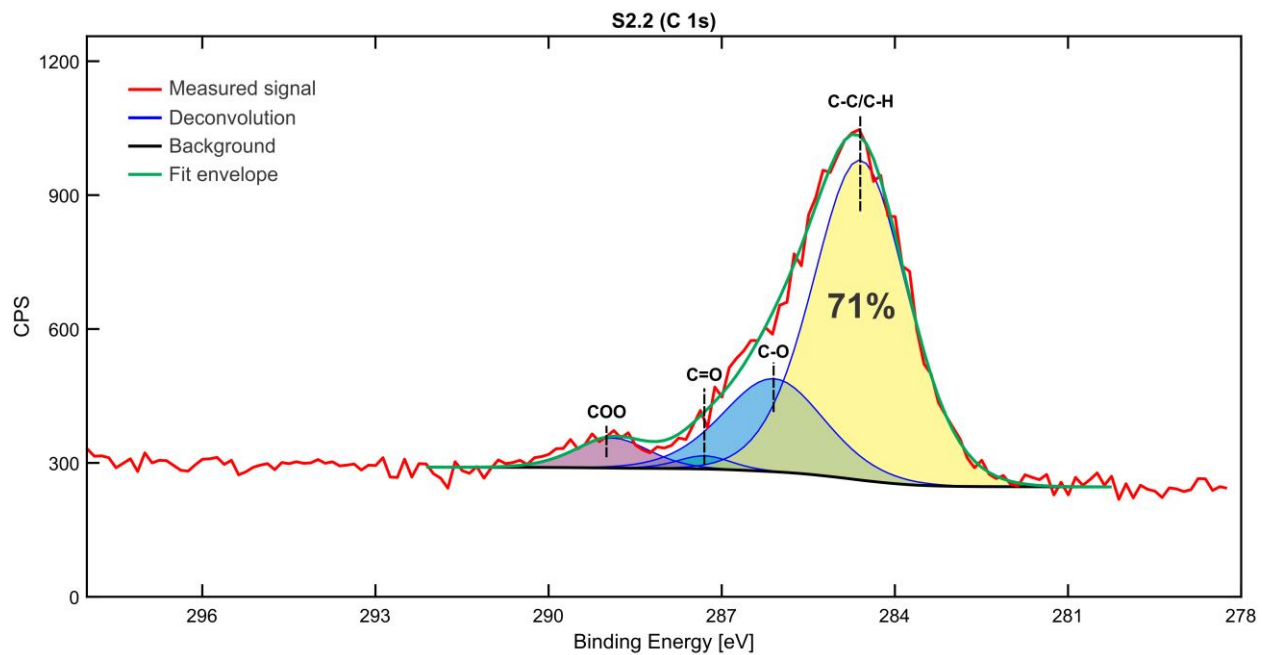
Figure S22. XPS spectrum of the C 1s peak on the sample S2.2.
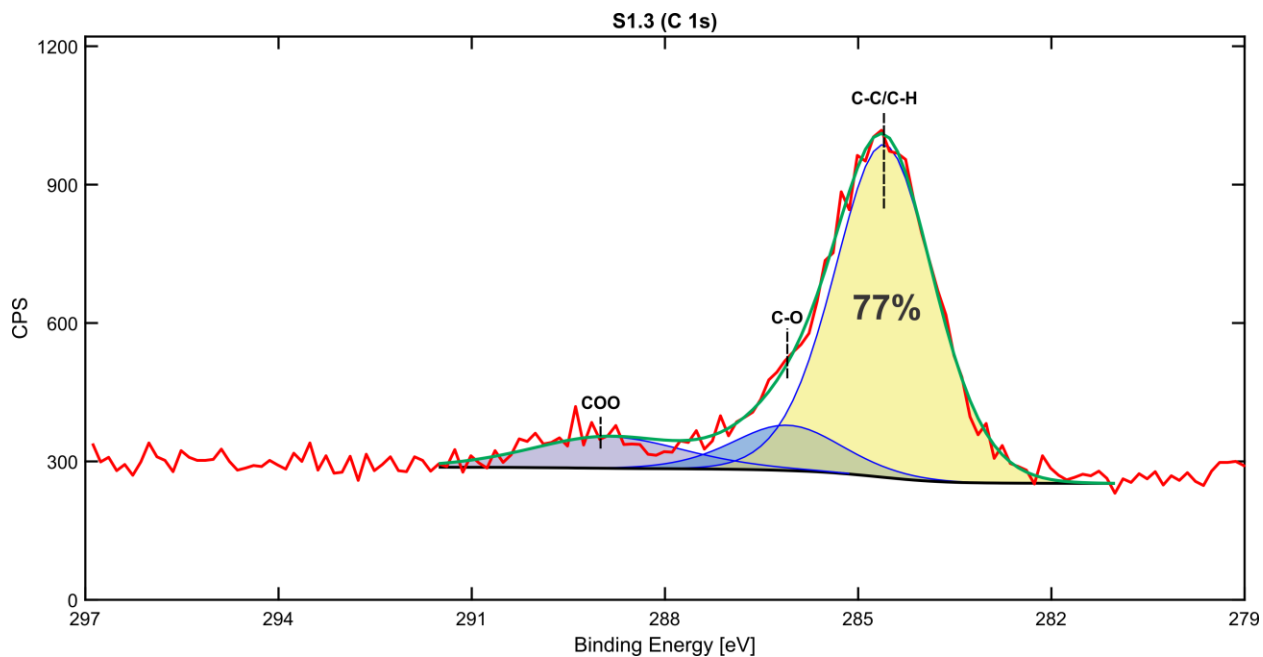
Figure S23. XPS spectrum of the C 1s peak on the sample S1.3.
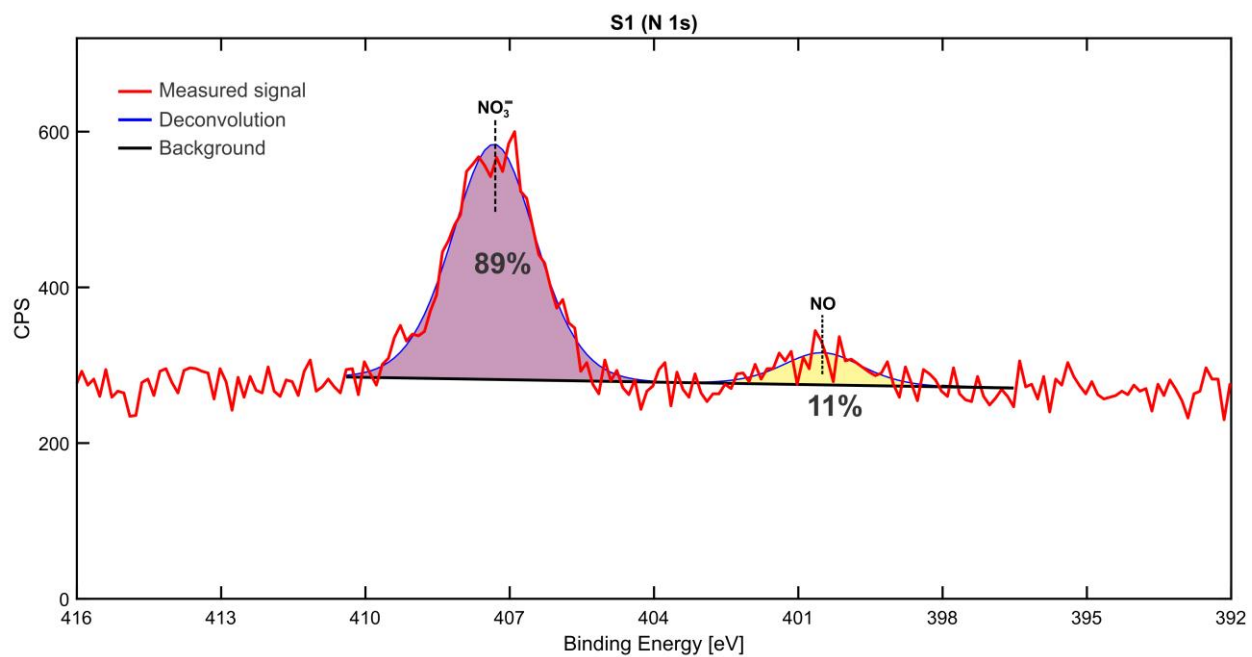
Figure S24. XPS spectrum of the N 1s peak on the sample S1.
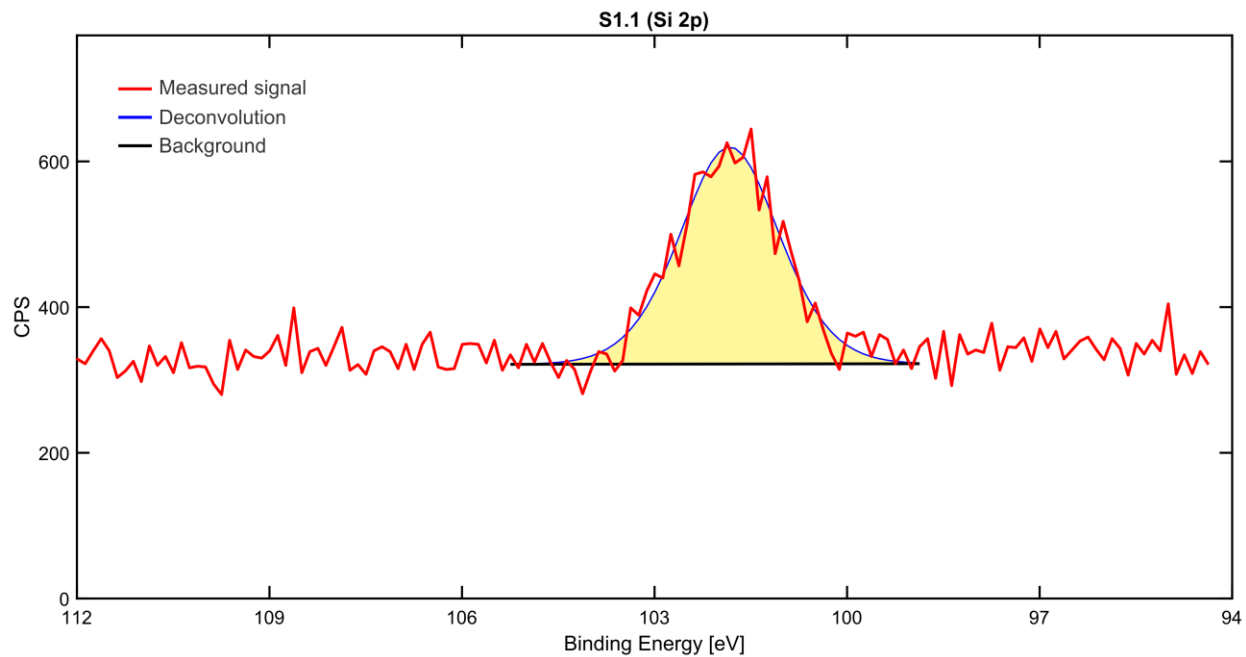
Figure S25. XPS spectrum of the Si 2p peak on the sample S1.1.
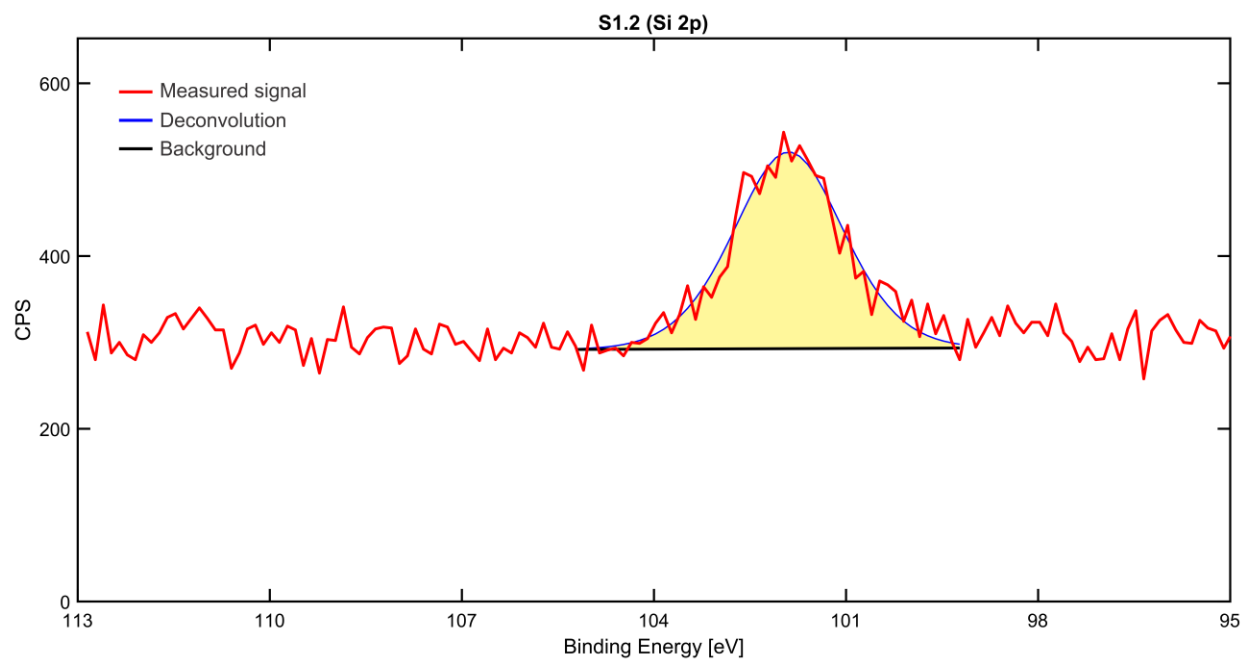
Figure S26. XPS spectrum of the Si 2p peak on the sample S1.2.
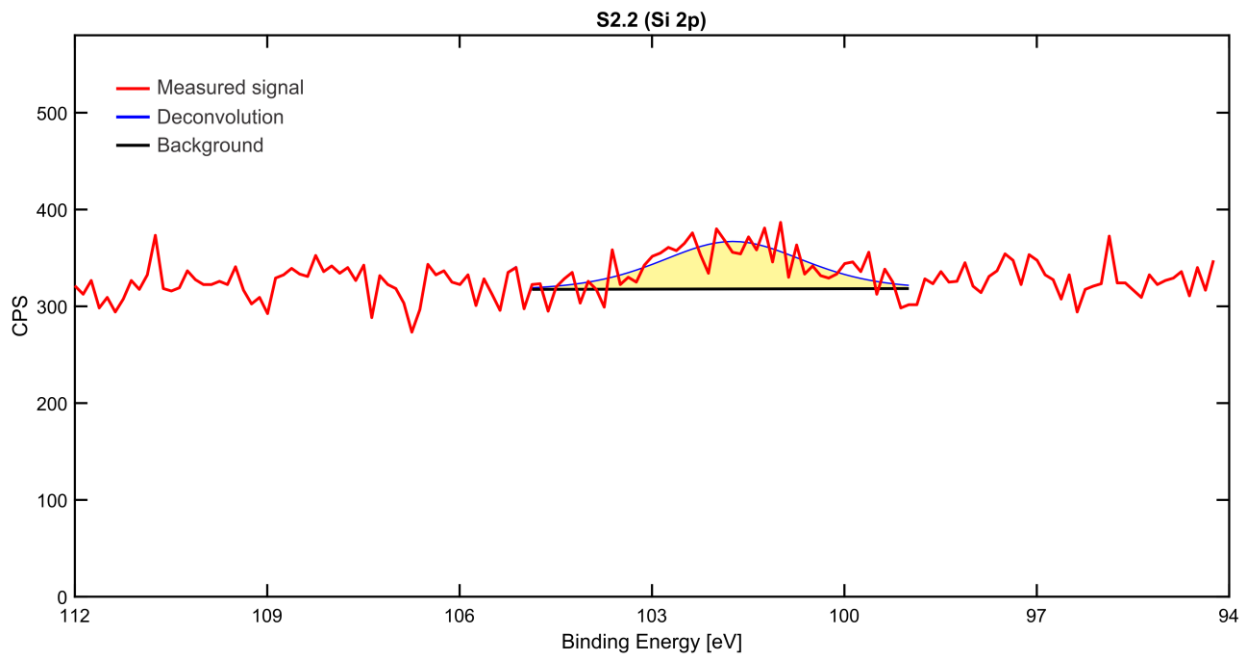
Figure S27. XPS spectrum of the Si 2p peak on the sample S2.2.
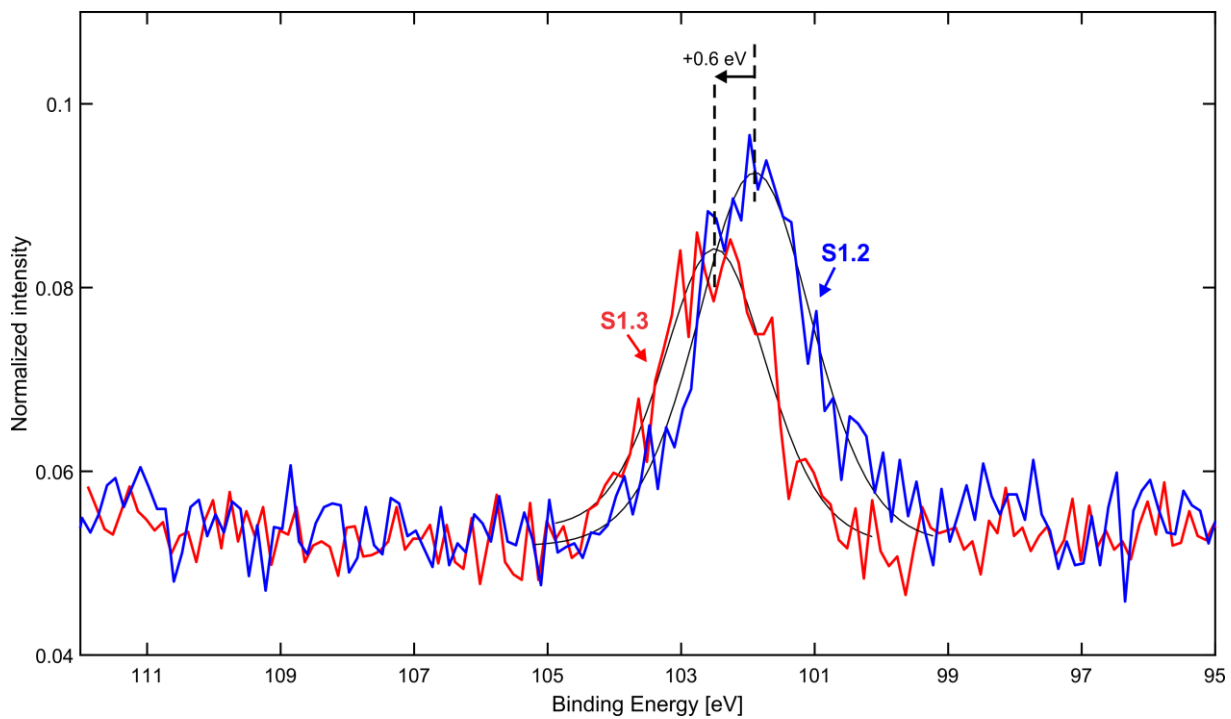
Figure S28. XPS spectrum of the Si 2p peaks on the samples S1.2 (the blue curve) and S1.3 (the red curve). The peak shifts for 0.6 eV towards higher binding energy after 2-h-long annealing at 350 °C.

Table S4. Concentration (in at. %) of the analyzed elements. The contact (CA) and roll-off angles (RoA), measured before the XPS analysis are shown for comparison.

| Sample		Ti 2p	C 1s	O 1s	Si 2p	N 1s	CA*	RoA*
S1	*as prepared*	24.5	20.0	51.9	0.0	3.3	0°	NA
	Ar+ sputtered	38.1	2.2	59.6	0.0	0.0		
S1.1	*as prepared*	25.8	22.9	48.2	3.1	0.0	156.6°± 2.5°	20.3° ± 3°
	Ar+ sputtered	30.3	8.1	59.2	2.4	0.0		
S1.2	*as prepared*	26.4	21.5	49.1	2.9	0.0	152.8°± 1.9°	NA
	Ar+ sputtered	33.1	6.6	58.7	1.6	0.0		
S2.2	*as prepared*	31.0	17.0	51.4	0.6	0.0	0°	NA
	Ar+ sputtered	31.1	4.9	64.0	0.0	0.0		
S1.3	*as prepared*	30.9	11.8	54.9	2.4	0.0	0°	NA
	Ar+ sputtered	34.8	2.7	60.8	1.8	0.0		

* S1.1 from *Period #2*, sample A (see the raw data in Tables S2 and S3); S1.2 from *Period #2*, sample B (see the raw data in Tables S2 an S3).

Table S5. C-C/C-H concentration (in at. %) in C 1s peak. The contact and roll-off angles, measured before the XPS analysis are shown for comparison.

Sample	S1	S1.1*	S1.2**	S2.2	S1.3
C-C/C-H Concentration	83.9	81.2	72.3	71.0	77.2
Contact Angle	0°	156.6°± 2.5°	152.8°± 1.9°	0°	0°
Roll-off Angle	NA	20.3° ± 3°	NA	NA	NA

* S1.1 from *Period #2*, sample A (see the raw data in Tables S2 and S3).
** S1.2 from *Period #2*, sample B (see the raw data in Tables S2 an S3).

Table S6. Ratios between concentrations, listed in Table S4 for the as-prepared samples.

Sample	O/Ti	C/Ti	Si/Ti	N/Ti
S1	2.1	0.8	0.0	0.1
S1.1	1.9	0.9	0.1	0.0
S1.2	1.9	0.8	0.1	0.0
S2.2	1.7	0.5	0.0	0.0
S1.3	1.8	0.4	0.1	0.0

S6 ToF-SIMS Analysis

To confirm that the Si 2p XPS photopeak really appears due to the PDMS contamination, samples S1.1 and S1.3 were additionally analyzed by the time-of-flight secondary ion mass spectroscopy (ToF-SIMS). 2D maps of the integrated intensity corresponding to $Si_3C_5H_{15}O_3^+$, $Si_2C_5H_{15}O^+$ and $SiC_3H_9^+$ secondary ions, acquired at two 0.5×0.5 mm^2 areas (512×512 pixels) on the sample S1.1 are shown in Figure S29. The results confirm that the sample is homogeneously covered by a thin film of a hydrophobic PDMS contaminant following annealing in Furnace #1.

The area normalized by the total ion intensity of the peaks for the selected secondary ions is shown in Table S7. The ratios between the same secondary ions detected on the sample S1.1 and S1.3 are also shown and confirm that the PDMS is oxidized at 350 °C in Furnace #3 (the shaded region in the last two columns of Table S7).
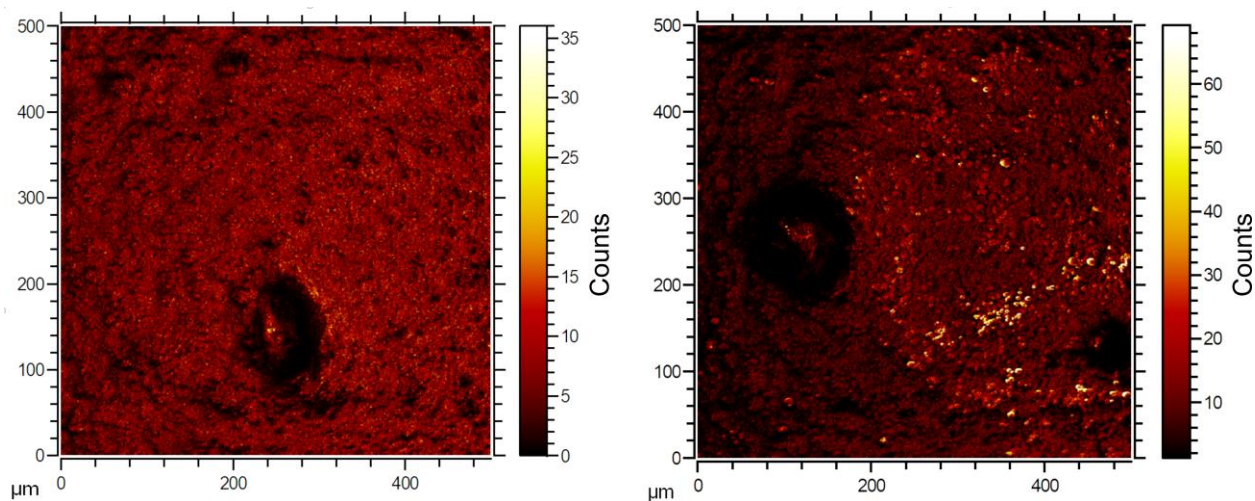
Figure S29. ToF-SIMS 2D maps taken on two different regions of the S1.1 sample displaying the integrated intensity of the $Si_3C_5H_{15}O_3^+$, $Si_2C_5H_{15}O^+$ and $SiC_3H_9^+$ secondary ions.

Table S7. Normalized intensities of the ToF-SIMS peaks corresponding to the selected secondary ions.

Secondary Ion	S1.1 Intensity [a.u.]	S1.3 Intensity [a.u.]	S1.1 Intensity, normalized by S1.3 Intensity	S1.3 Intensity, normalized by S1.1 Intensity
SiO_3^-	0.00466	0.03750	0.1	8.0
$SiHO_3^-$	0.00604	0.04050	0.1	6.7
$Si_2O_5^-$	0.00029	0.00106	0.3	3.6
$Si_2HO_5^-$	0.00087	0.00302	0.3	3.5
$SiCH_3O^-$	0.00175	0.00555	0.3	3.2
SiO_2^-	0.01790	0.03470	0.5	1.9
$SiHO_2^-$	0.00581	0.00791	0.7	1.4
Si^+	0.00846	0.00711	1.2	0.8
$SiCH_5^+$	0.00459	0.00159	2.9	0.3
Si^-	0.00073	0.00024	3.1	0.3
$SiC_3H_9^+$	0.03400	0.00420	8.1	0.1
$SiCH_3O_2^-$	0.01100	0.00129	8.5	0.1
$Si_3C_5H_{15}O_3^+$	0.00184	0.00016	11.4	0.1
$Si_2C_5H_{15}O^+$	0.00601	0.00050	12.1	0.1

S7 Light Reflection from the Metallic Surface

For the idealized physical model based on the classical theory of the electron, the basic equations relating to the electromagnetic propagation in metals (i.e., a conducting medium) differ from those describing the propagation in transparent dielectrics *only* in that the real refractive index n is replaced by a complex refractive index:[S10]

$$\hat{n} = n + i\kappa \tag{S1}$$

where n and κ (the extinction coefficient) are real.

The Snell's law of refraction still reads as:

$$\sin\theta_t = \frac{1}{\hat{n}}\sin\theta_i \tag{S2}$$

where θ_i and θ_t stand for the incident and transmitted angles, respectively. Since $\hat{n}$ is complex, the quantity θ_t is also complex.

By introducing Equations (S1) and (S2), the well-known Fresnel equations for the reflectivity coefficients of the perpendicular (s, called also TE) and parallel (p, called also TM) polarizations of the *electromagnetic field* are still valid:

$$r_p = \frac{\tan(\theta_i - \theta_t)}{\tan(\theta_i + \theta_t)} \tag{S3}$$

$$r_s = -\frac{\sin(\theta_i - \theta_t)}{\sin(\theta_i + \theta_t)} \tag{S4}$$

The *complex* coefficients r_p and r_s can be expressed by the absolute values of the reflection coefficients ρ_p, ρ_s and by phase changes induced by reflection ϕ_p, ϕ_s:

$$r_p = \rho_p e^{i\phi_p} \tag{S5}$$

$$r_s = \rho_s e^{i\phi_s} \tag{S6}$$

The reflectance for the *intensity* (or *power*) is calculated as:

$$R_{p,s} = r_{p,s} r_{p,s}^* = \left| r_{p,s} \right|^2 \qquad \text{(S7)}$$

where the asterisk denotes the complex conjugate.

In case of the unpolarized light (up), the *intensity* (or *power)* reflectance is the arithmetic mean of the intensity reflectance for both polarizations:

$$R_{up} = \frac{R_s + R_p}{2} \qquad \text{(S8)}$$

For normal incidence ($\theta_i = 0°$), $r_s = r_p$ and the intensity reflection is expressed as:

$$R_{normal} = \frac{\left(n_0 - n_{me}\right)^2 + \kappa_{me}^2}{\left(n_0 + n_{me}\right)^2 + \kappa_{me}^2} \qquad \text{(S9)}$$

where indices 0 and "me" denote air and metal, respectively.

Lian et al.[S1] measured the spectrum of the light reflected from their (unprocessed) flat titanium surface. This spectrum is shown by the black curve in Figure S30. Several authors[S11-S14] have measured the refractive index of pure titanium as a function of the wavelength. The theoretical reflectivity, calculated from this data using Equation (S9), is shown by the color curves in Figure S30a for a comparison with the results obtained by Lian et al.[S1] (the black curve).

It is clearly evident from Figure S30a that all the data from the literature results in higher reflectivity as measured in Ref.[S1] and that none of the colored curves have the same trend as a function of the wavelength. There are several reasons for this. The spectra, presented by the color curves, were measured on pure titanium with special care taken to minimize the surface oxidation. On the contrary, the sample in Ref.[S1] was oxidized and contained only 87% of titanium (in fact it can be classified as Ti-6Al-4V titanium alloy) and – most probably – it was also not perfectly smooth, but it contained some roughness. However, for further supplementary calculations, the

refractive index reported by Mash and Motulevich[S13] is used since the reflectance from their data is the most similar to the measurements from Ref.[S1] (see Figure 30b).

The average reflectivity in the 400 nm–1000 nm range calculated from Ref.[S13] (the dark green curve in Figure S30a) equals $R_{theor.} = 0.55$, while the average reflectivity, measured by Lian et al.[S1] (the black curve in Figure S30) equals $R_{meas.} = 0.41$. The scaling factor $\beta = R_{meas.}/R_{theor.} = 0.8$ was used to scale the theoretical curve in Figure S30b.
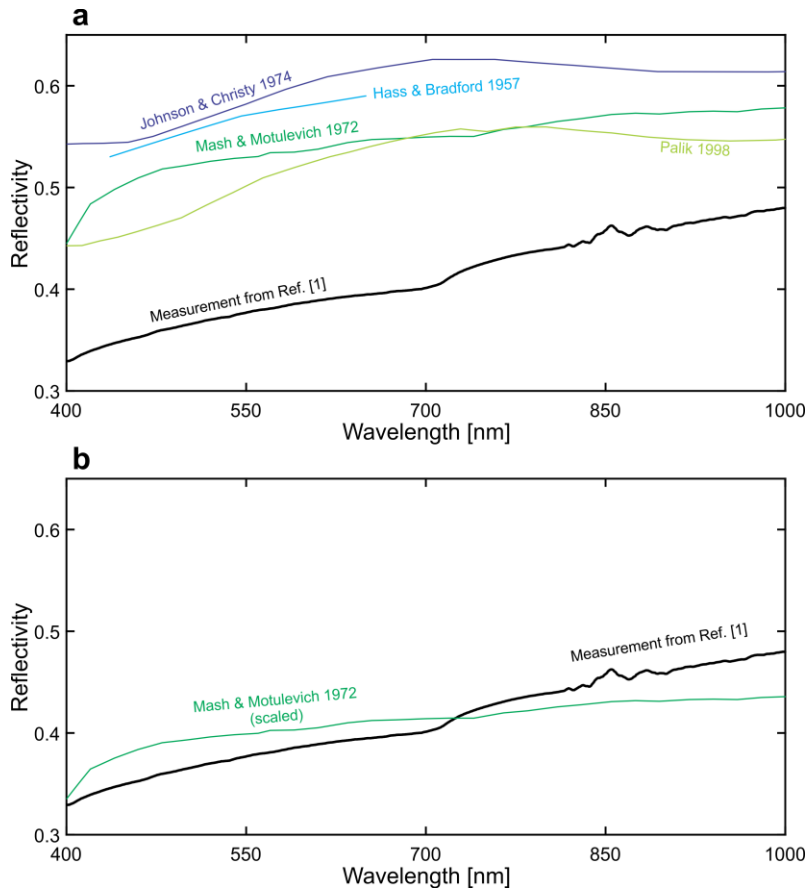
Figure S30. Reflectivity of titanium as a function of the wavelength for normal incidence ($\theta_i = 0°$). The data reported by Lian et al.[S1] for the unprocessed surface is marked by the black solid curve. **a** The color curves show the calculated spectra [using Equation (S9)] for the refractive indices of titanium measured by Johnson and Christy,[S11] Hass and Bradford,[S12] Mash and Motulevich[S13] and reviewed by Palik.[S14] **b** Reflectivity for titanium, calculated by using data from Ref.[S13] and scaled to the measurement by Lian et al.[S1]

S8 Light Reflection from the Metallic Surface Covered by a Single Thin-Film Layer

When a metallic surface is covered by a thin oxide layer, the interference effects due to light reflections from the air-oxide and oxide-metal interfaces should not be neglected.[S12] In this case, the reflection can be modeled, as is schematically shown in Figure S31.

The amplitude of the reflected electric field E_r is a sum of all reflected beams and the ratio between the amplitudes of the reflected E_r and the incident electric field E_i can be calculated as:

$$\frac{E_r}{E_i} = r_{12} + t_{12}r_{23}t_{21}e^{i\delta_{ox}} + t_{12}r_{23}^2r_{21}t_{21}e^{2i\delta_{ox}} + t_{12}r_{23}^3r_{21}^2t_{21}e^{3i\delta_{ox}} + \cdots \qquad (S10)$$

where index "ox" denotes the titanium (di)oxide, while indices 1, 2 and 3 stand for the first medium (air), the second medium (titanium (di)oxide) and the third medium (titanium), respectively.

The difference in optical path between the ray that is reflected from the oxide film with thickness d_{ox} and the ray, reflected from the metallic surface equals $2d_{ox}\hat{n}_{ox}\cos(\theta_{ox})$. Thus, the phase change shift on passing through the oxide film in Equation (S10) equals:

$$\delta_{ox} = \frac{4\pi d_{ox}}{\lambda}\hat{n}_{ox}\cos(\theta_{ox}) \qquad (S11)$$

where λ stands for the wavelength of light in vacuum and θ_{ox} is obtained from the incident angle θ_i using Equation (S2).

Using the following identities:

$$r_{21} = -r_{12} \qquad (S12)$$

$$t_{12}t_{21} + r_{12}^2 = 1 \qquad (S13)$$

the Equation (S10) can be written as:

$$\frac{E_r}{E_i} = r_{12} + \left(1 - r_{12}^2\right)\sum_{m=1}^{\infty}(-1)^{m+1}r_{12}^{m-1}r_{23}^m e^{im\delta_{ox}} \qquad (S14)$$

The reflectance r_{STF} for the electric field, when the metal is covered by a *single* thin film (STF) [Equation (S14)] can be presented in the following form:[S15]

$$r_{\text{STF}} = \frac{r_{12} + r_{23}\,\mathrm{e}^{\mathrm{i}\delta_{\text{ox}}}}{1 + r_{12}r_{23}\,\mathrm{e}^{\mathrm{i}\delta_{\text{ox}}}} \tag{S15}$$

Note that Equation (S15) already considers the light absorption in the oxide film if a complex refractive index $\hat{n}_{\text{ox}}$ is used. In this case, the exponential term in Equation (S15) can be deconvoluted into imaginary and real component as:

$$\mathrm{e}^{\mathrm{i}\delta_{\text{ox}}} = \mathrm{e}^{\mathrm{i}\frac{4\pi d_{\text{ox}}\cos(\theta_{\text{ox}})}{\lambda}(n_{\text{ox}}+\mathrm{i}\kappa_{\text{ox}})} = \mathrm{e}^{\mathrm{i}\frac{4\pi d_{\text{ox}}\cos(\theta_{\text{ox}})}{\lambda}n_{\text{ox}}}\,\mathrm{e}^{-\frac{4\pi d_{\text{ox}}\cos(\theta_{\text{ox}})}{\lambda}\kappa_{\text{ox}}} \tag{S16}$$

Here, the term $4\pi\kappa_{\text{ox}}/\lambda = \mu_{\text{ox}}$ is the Lambert absorption coefficient for the oxide. Thus, relation in Equation (S16) for normal incidence reads as:

$$\mathrm{e}^{\mathrm{i}\delta_{\text{ox}}} = \mathrm{e}^{\mathrm{i}\frac{4\pi d_{\text{ox}}}{\lambda}n_{\text{ox}}}\,\mathrm{e}^{-\mu_{\text{ox}}d_{\text{ox}}} \tag{S17}$$

The first (imaginary) part on the right-hand side in Equations (S16)−(S17) represents the phase change, while the second (real) part determines the light absorption.

To calculate the electromagnetic field reflectance r_{STF} for different polarizations, the coefficients r_{ij} in Equation (S15) are calculated for the s and p polarized light using Equations (S3) and (S4). The intensity reflectance is further calculated by Equations (S7) and (S8).
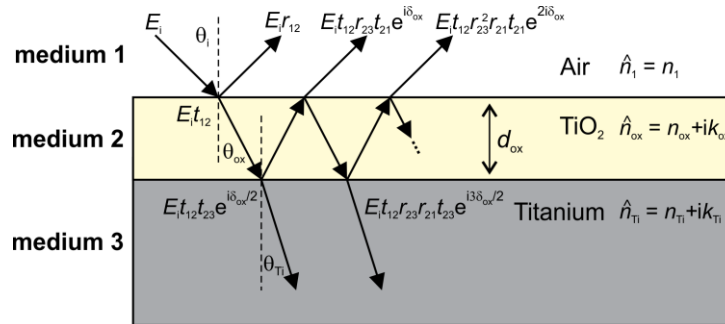
Figure S31. Schematic representation of the reflectance of the electric field from a thin oxide layer on the bulk titanium surface.

S9 Light Reflection from the Metallic Surface Covered by Double Thin-Film Layer

When the oxidized titanium surface is additionally covered by a water layer, this results in a *double* thin-film system (DTF), which is schematically shown in Figure S32.

In this case the reflectance for the electric field can be calculated as:[S16]

$$r_{DTF} = \frac{r_{12} + r_{23}\,e^{i\delta_w} + r_{34}\,e^{i(\delta_w + \delta_{ox})} + r_{12}r_{23}r_{34}\,e^{i\delta_{ox}}}{1 + r_{12}r_{23}\,e^{i\delta_w} + r_{12}r_{34}\,e^{i(\delta_w + \delta_{ox})} + r_{23}r_{34}\,e^{i\delta_{ox}}} \tag{S18}$$

In Equation (S18), δ_w and δ_{ox} are calculated by Equation (S11). The indices "w" and "ox" stand for the thin film of water and the titanium dioxide, respectively.

Similarly, as in case of Equation (S15), the Equations (S3), (S4), (S7) and (S8) are used to calculate the intensity reflectance from the electric field reflectivity given by Equation (S18).
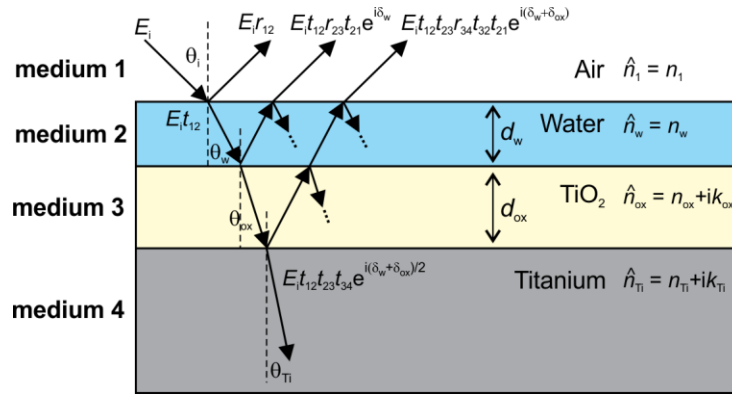
Figure S32. Schematic representation of the reflectance and transmittance of the electric field from the air-water, water-oxide and oxide-titanium interfaces.

S10 References

(S1)   Lian, Z.; Xu, J.; Yu, Z.; Yu, P.; Ren, W.; Wang, Z.; Yu, H. Bioinspired Reversible Switch between Underwater Superoleophobicity/Superaerophobicity and Oleophilicity/Aerophilicity and Improved Antireflective Property on the Nanosecond Laser-Ablated Superhydrophobic Titanium Surfaces. *ACS Appl. Mater. Interfaces* **2020,** *12* (5), 6573-6580.

(S2)   McHale, G.; Shirtcliffe, N. J.; Newton, M. I. Super-hydrophobic and super-wetting surfaces: Analytical potential? *Analyst* **2004,** *129* (4), 284-287.

(S3)   Marmur, A. Hydro- hygro- oleo- omni-phobic? Terminology of wettability classification. *Soft Matter* **2012,** *8* (26), 6867-6870.

(S4)   Gregorčič, P.; Šetina-Batič, B.; Hočevar, M. Controlling the stainless steel surface wettability by nanosecond direct laser texturing at high fluences. *Appl. Phys. A: Mater. Sci. Process.* **2017,** *123* (766), 1-8.

(S5)   Ketteler, G.; Yamamoto, S.; Bluhm, H.; Andersson, K.; Starr, D. E.; Ogletree, D. F.; Ogasawara, H.; Nilsson, A.; Salmeron, M. The nature of water nucleation sites on TiO2(110) surfaces revealed by ambient pressure X-ray photoelectron spectroscopy. *J. Phys. Chem. C* **2007,** *111* (23), 8278-8282.

(S6)   Rosseler, O.; Sleiman, M.; Montesinos, V. N.; Shavorskiy, A.; Keller, V.; Keller, N.; Litter, M. I.; Bluhm, H.; Salmeron, M.; Destaillats, H. Chemistry of NOx on TiO2 Surfaces Studied by Ambient Pressure XPS: Products, Effect of UV Irradiation, Water, and Coadsorbed K+. *J. Phys. Chem. Lett.* **2013,** *4* (3), 536-541.

(S7)   Long, J. Y.; Zhong, M. L.; Fan, P. X.; Gong, D. W.; Zhang, H. J. Wettability conversion of ultrafast laser structured copper surface. *J. Laser Appl.* **2015,** *27,* S29107.

(S8)   Jeong, M. G.; Seo, H. O.; Kim, K. D.; Kim, Y. D.; Lim, D. C. Enhanced photocatalytic activity of TiO2 by polydimethylsiloxane deposition and subsequent thermal treatment at 800 degrees C. *Thin Solid Films* **2012,** *520* (15), 4929-4933.

(S9)   Glasmastar, K.; Gold, J.; Andersson, A. S.; Sutherland, D. S.; Kasemo, B. Silicone transfer during microcontact printing. *Langmuir* **2003,** *19* (13), 5475-5483.

(S10)   Born, M.; Wolf, E. *Principles of optics;* Cambridge University Press: Cambridge, U.K., 2005.

(S11)   Johnson, P. B.; Christy, R. W. Optical-Constants of Transition-Metals - Ti, V, Cr, Mn, Fe, Co, Ni, and Pd. *Phys. Rev. B* **1974,** *9* (12), 5056-5070.

(S12)   Hass, G.; Bradford, A. P. Optical Properties and Oxidation of Evaporated Titanium Films. *J. Opt. Soc. Am.* **1957,** *47* (2), 125-129.

(S13)   Mash, I. D.; Motulevich, G. P. Optical-Constants and Electron Characteristics of Titanium. *Zh. Eksp. Teor. Fiz.* **1972,** *63* (3), 985-992.

(S14)   Palik, E. D. *Handbook of Optical Constants of Solids*; Academic Press: New York, 1998.

(S15)   Nestell, J. E.; Christy, R. W. Optics of Thin Metal Films. *Am. J. Phys.* **1971,** *39* (3), 313-320.

(S16)   Łęcka, K. M.; Wójcik, M. R.; Antończak, A. J. Laser-Induced Color Marking of Titanium: A Modeling Study of the Interference Effect and the Impact of Protective Coating. *Math. Probl. Eng.* **2017**, *2017,* 1.